Modern Physics Letters A
© World Scientific Publishing Company

arXiv:1404.6484v1 [hep-ex] 25 Apr 2014

CHARGED CURRENT QUASI-ELASTIC CROSS SECTION MEASUREMENTS IN MINIBOONE

JOSEPH GRANGE *

Department of Physics, University of Florida,
Gainesville, FL 32611, U.S.A.
jgrange@phys.ufl.edu

TEPPEI KATORI †

Laboratory for Nuclear Science, Massachusetts Institute of Technology,
Cambridge, MA 02139, U.S.A.
katori@mit.edu

Received (Day Month Year)
Revised (Day Month Year)

The neutrino-induced charged-current quasi-elastic (CCQE, $\nu_l + n \to l^- + p$ or $\bar{\nu}_l + p \to l^+ + n$) interaction is the most abundant interaction around 1 GeV, and it is the most fundamental channel to study neutrino oscillations. Recently, MiniBooNE published both muon neutrino[1], and muon anti-neutrino[2] double differential cross sections on carbon. In this review, we describe the details of these analyses and include some historical remarks.

Keywords: MiniBooNE; neutrino oscillation; CCQE;

PACS: 11.30.Cp, 14.60.Pq, 14.60.St

1. MiniBooNE experiment

The Mini Booster Neutrino Experiment (MiniBooNE) (2002-2012) is designed to detect ν_e ($\bar{\nu}_e$) appearance signals from ν_μ ($\bar{\nu}_\mu$) beam in $\Delta m^2 \sim 1\text{eV}^2$ region through charged current quasi-elastic (CCQE) interactions.

$$\nu_\mu \overset{oscillation}{\longrightarrow} \nu_e + n \to e^- + p \ ,$$
$$\bar{\nu}_\mu \overset{oscillation}{\longrightarrow} \bar{\nu}_e + p \to e^+ + n \ .$$

Confirmation of such an oscillation signal would indicate new physics beyond the Standard Model, such as sterile neutrinos. To test for the existence of exotic mixing with $\Delta m^2 \sim 1\text{eV}^2$, the MiniBooNE experiment was designed to observe

*Present address: Argonne National Laboratory, Argonne, IL, 60439, U.S.A, grange@anl.gov
†Present address: Queen Mary University of London, London, E1 4NS, U.K, t.katori@qmul.ac.uk

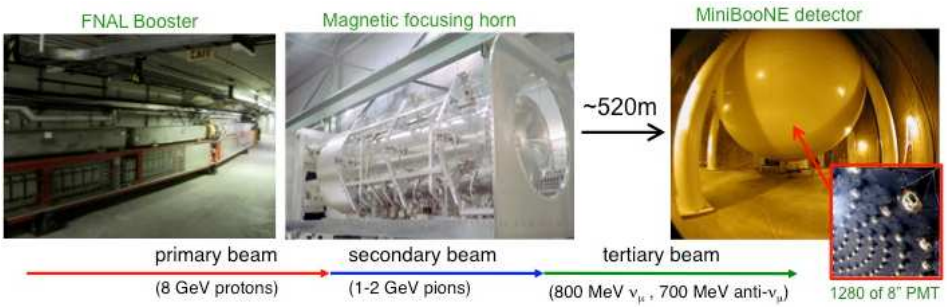

Fig. 1. The scheme of the MiniBooNE experiment. Protons (primary beam) are extracted from Fermilab Booster, then send to the target located in the magnetic focusing horn to create shower of mesons (secondary beam). Neutrinos are produced by decay-in-flight of mesons (tertiary beam), and detected by the MiniBooNE detector.

neutrino interactions with E_ν ~800 MeV in a mineral oil based Cherenkov detector at a baseline L~500 m. The energy and baseline values are chosen so that the ratio L/E_ν matches the signal reported previously by the LSND experiment[3]. This allows sensitivity to the same Δm^2 region under the two-neutrino massive oscillation model.

In order to reliably predict the appearance of ν_e and $\bar{\nu}_e$, it is crucial to first understand in detail the rate and kinematics of ν_μ and $\bar{\nu}_\mu$ interactions. This is particularly true in a single-detector experiment such as MiniBooNE, where these physics samples serve as an important constraint. Assuming lepton universality, ν_μ ($\bar{\nu}_\mu$) CCQE interactions should be identical to ν_e ($\bar{\nu}_e$) CCQE interactions, with the exception of effects arising from the charged lepton mass. This supposedly simple interaction is the subject of this review article. Due to nuclear effects, we find rich nature in this interaction not previously considered in neutrino experiments.

In this section we give an overview of the MiniBooNE experiment. In the following section (Sec. 2), we discuss the neutrino beam, the heart of all neutrino cross section measurements. The general method of cross section analysis is described in Sec. 3, and Sec 4 begins the discussion of the MiniBooNE ν_μ CCQE measurement. CCQE interactions with the $\bar{\nu}$-mode beam is discussed in the following section (Sec. 5), and Sec. 6 describes the combined result. The conclusions follow.

1.1. *Booster neutrino beamline (BNB)*

MiniBooNE accepts muon (anti)neutrino beam from the Fermilab Booster neutrino beamline (BNB) [4]. Fig. 1 shows the scheme of the BNB. The 8 GeV primary proton beam is extracted from the Booster and steered to collide with the beryllium target in the magnetic focusing horn. The collision of protons with the target creates a shower of secondary mesons, and the polarity of the surrounding toroidal field is chosen to focus $\pi^+(\pi^-)$ for $\nu(\bar{\nu})$ mode. The horn simultaneously defocuses $\pi^-(\pi^+)$ to reduce the backgrounds from $\bar{\nu}_\mu(\nu_\mu)$ interactions in $\nu(\bar{\nu})$ mode beam. The decay-

in-flight of the sign-selected $\pi^+(\pi^-)$ in an air-filled hall leads to a tertiary beam composed mostly of $\nu_\mu(\bar{\nu}_\mu)$. The decay length of typical pions are ∼18 m. This wideband $\nu_\mu(\bar{\nu}_\mu)$ beam is peaked around 800 (650) MeV.

1.2. *MiniBooNE detector*

The MiniBooNE detector is located 541 m north of the target[5]. The detector is a 12.2 m diameter spherical Cherenkov detector filled with 800 tons of undoped mineral oil, whose chemical composition is dominantly CH_2. An inner region with diameter 11.5 m is covered with 1,280 8-inch PMTs (Fig. 1) and is optically separated from the 35 cm thick outer shell which houses 240 8-inch PMTs and acts as a veto to identify both exiting and entering charged particles.

The PMT timing information is used to associate clusters of activity with the signature of a single particle using PMT "hits", and temporal groups of hits form "subevents". With high efficiency, subevents are used to identify and separate particles whose transit emits significant amounts of Cherenkov light and so are excellent for separating the signature and topology of muons from their decay electrons in CCQE interactions (Fig. 2, left).

The primary result of the analyses described here is the flux-integrated differential cross section of muon (anti-muon) kinematics from the CCQE interaction.

$$\nu_\mu + n \to \mu^- + p \ ,$$
$$\bar{\nu}_\mu + p \to \mu^+ + n \ .$$

Figure 2, right, shows a cartoon of this reaction. We identify muon (anti-muon) by detecting first subevent from the muon (anti-muon) and delayed second subevent from the electron (positron). This two-fold signal defines the CCQE interaction. Details of signal definition and event selections are given in Sec. 3.1 and Sec. 3.2.

A natural advantage of the MiniBooNE Cherenkov detector technology is its angular acceptance of the muon produced in CCQE interactions. The spherically symmetric geometry allows for equal angular acceptance over the full 4π of solid angle. This is in contrast to forward type tracking detectors. The acceptance of tracking detectors is necessarily a function of the production angle, where muons created perpendicular to the neutrino direction are almost entirely missed, and backwards-going muons can be very challenging to reconstruct[6]. This is much more than just an experimental detail; the physics reach of a given detector is highly dependent on the angular acceptance.

1.3. *Event reconstruction*

The pattern, timing, and total charge of prompt Cherenkov radiation collected by the PMTs is used to identify particle type and its kinematics, which is the direct observable of the experiment and forms the basis of the differential cross sections [7].

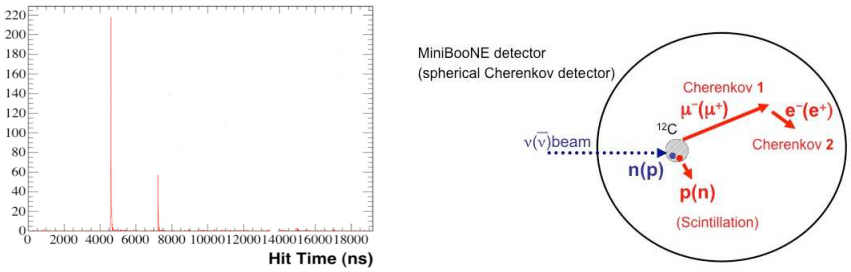

Fig. 2. Left plot shows a data hit distribution for two subevents. The first high peak corresponds to muon Cherenkov ring, and the subsequent small peak corresponds to the Cherenkov radiation from the electron following muon decay. Right cartoon shows the CCQE interaction in MiniBooNE detector. The muon (anti-muon) produces the primary Cherenkov ring, which is characterised with higher hits, then subsequent decay produces weaker secondary Cherenkov ring from the electron (positron). Nucleons are often below Cherenkov threshold and ignored. Notice hydrogen atoms also participate in CCQE for muon anti-neutrino interactions.

For the $\nu_\mu(\bar{\nu}_\mu)$ CCQE cross section measurements described in this review, we identify muon tracks and their kinematics from CCQE interactions. To determine these crucial quantities, a likelihood function is compared to the topology and timing of the observed PMT hits:

$$\mathcal{L}(\mathbf{x}) = \prod_{\text{unhit PMTs } i} (1 - P(i\,\text{hit};\mathbf{x})) \times \prod_{\text{hit PMTs } i} P(i\,\text{hit};\mathbf{x})\, f_q(q_i;\mathbf{x})\, f_t(t_i;\mathbf{x}), \quad (1)$$

where $P(i\,\text{hit};\mathbf{x})$ is the probability for PMT i to register a hit given the muon vertex and kinematic vector $\mathbf{x}$, and f_q (f_t) is a probability distribution function (PDF) for the hit to return the measured charge (time) q_i (t_i) operating under a muon hypothesis.

The vector $\mathbf{x}$ is composed of the muon time, energy and position at creation, as well as its momentum projections along the spherical azimuthal and polar angles. The negative logarithm of the likelihood function in Eq. 1 simultaneously varies these seven parameters while comparing to the observed PMT hits. The parameters from the maximised likelihood function yield the reconstructed muon kinematics.

Such likelihood function is also developed for other particles, and used for cross section measurements beyond the CCQE interactions, including neutral current π^0 production [8], neutral current elastic scattering [9,10], charged-current π^+ production [11], and charged-current π^0 production [12]. Indeed, MiniBooNE measured over 90% of all possible muon neutrino interactions in the MiniBooNE detector.

2. Neutrino flux

Neutrino cross sections have been measured since the advent of the high intensity neutrino beam[13]. The observable is the rate of the interaction. This can be described

by the convolution of the neutrino flux (Φ), the neutrino interaction cross section (σ), and the experimental detection efficiency (ϵ).

$$rate \propto \int \Phi \times \sigma \times \epsilon \tag{2}$$

Clearly, we need to know the neutrino flux *a priori* to infer the cross section from the measurement of neutrino rates in the detector. This is in general not easy, since high intensity modern neutrino beams are made from decay-in-flight mesons.

Modern neutrino experiments typically rely heavily on the prediction of neutrino flux from simulations with varying degrees of data constraints. Typical simulations include (1) primary proton beam propagation, and interaction with target material, (2) production of secondary mesons, propagation and decay, and (3) tertiary neutrino beam prediction under suitable geometry setting.

2.1. *Primary proton interactions*

Historically, little attention is paid to the proton - target interaction model. However, there is a large uncertainty on this process, and even worse, those models are tuned from old and sparse data. Such proton interaction model contributes the large uncertainty to both BNB [14] and the T2K neutrino flux [15]. Clearly, these error estimates can and will be improved in the future as cross-section measurements move into an era of greater precision.

2.2. *Meson production cross section*

Since conventional high-intensity neutrino beams are made by decay-in-flight mesons, special attention is paid to the simulation of meson production. The program of choice for a reliable flux prediction involves dedicated external measurements of meson production, such as those provided by the HARP experiment for K2K and MiniBooNE. Figure 3, left, shows the drawing of the HARP detector [16]. These hadroproduction experiments use tracking detectors to measure outgoing meson kinematics as precisely as possible. Figure 3, right, shows the $p - \theta$ distribution of π^+ in the BNB (simulation) which produces muon neutrinos passing through the MiniBooNE detector. The red box shows the region measured by the HARP experiment. 81.1% of pions are directly measured, and outside of the box is extrapolated from the model.

2.3. *Forward-going mesons*

Even with dedicated hadroproduction data, regions of meson phase space crucial to neutrino experiments may not be available. Since non-interacting protons are undeflected, hadroproduction detectors at zero degrees relative to the proton beam become saturated and these regions are extremely challenging to measure. Therefore, mesons produced at very forward angles are often not reported, and neutrino

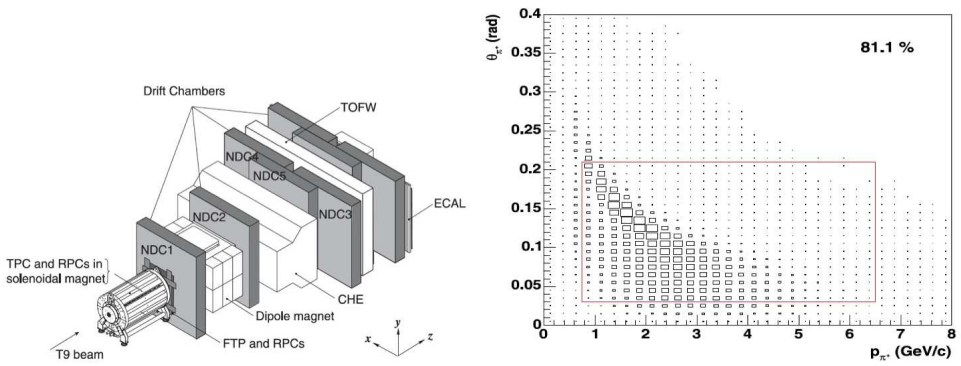

Fig. 3. The left plot show the HARP detector. The detector consists of different sub-detectors to improve particle ID. The right plot shows the $p-\theta$ distribution of π^+ in the BNB (simulation) which produces muon neutrinos passing through the MiniBooNE detector.

experiments must either extrapolate the data into this region or find external constraints. For the HARP experiment, this corresponds to pions below 0.03 rad (Fig. 3, right). As we will see in Sec. 5.2, such a situation demanded MiniBooNE use a variety of *in situ* measurements to measure the π^+ production cross section at low production angles to correct ν_μ induced backgrounds in the $\bar{\nu}$-mode beam.

2.4. *Proton re-scattering*

The nuclear target size is chosen to maximise primary proton interaction rate, and an accompanying complication is the possibility of proton scattering more than once as it traverses the material. The prediction of mesons produced in such interactions is known to be challenging, and unfortunately their contribution is typically not directly constrained by dedicated hadroproduction data.

Hadroproduction experiments usually extract meson production cross sections using "thin" nuclear targets, of proton interaction length $\sim$5%, while the target used in the experiment is usually close to 2 interaction lengths. Thus a significant fraction of protons are scattered more than once to create mesons. The left side of Figure 4 shows[18] the overall contribution of these processes to the total neutrino flux. For the BNB energy (8.9 GeV/c), this effect is rather low, and it is at the level of $\sim$ 10%. The right side of the same figure also suggests the contribution from pions due to re-scattering protons present in the full MiniBooNE target but not in the thin target data collected by HARP is small. Therefore, with the exception of the very forward-going angular region addressed in Sec. 5, the HARP data allows for a minimally model-dependent determination of the production of neutrino and anti-neutrino parent pions at the BNB. Note that proton re-scattering processes become more important with higher primary proton energy, such as MINERvA (using 120 GeV main injector), and T2K (30 GeV synchrotron ring).

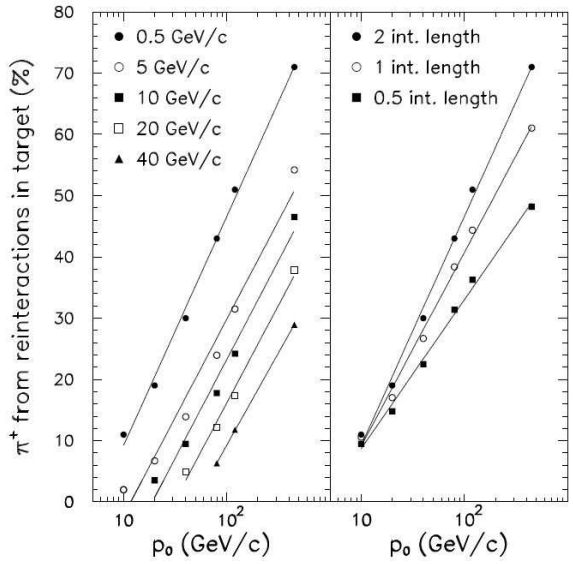

Fig. 4. Simulation of the tertiary π^+ yield from re-interactions in a graphite target. Given as a function of incident proton beam momentum p_0, the π^+ fraction is given for the indicated thresholds on the longitudinal component of the π^+ momentum (left), and also for targets of 0.5, 1.0, and 2.0 interaction lengths (right). The primary proton beam at the BNB has momentum 8.9 GeV/c.

2.5. *Neutrino flux data driven correction*

As Eq. 2 shows, a measurement is a convolution of neutrino flux and neutrino cross section model. Therefore, it is dangerous to tune the neutrino flux from the neutrino data, and this was incorrectly done in past experiments. For example, it was common to model the neutrino flux from the CCQE interaction measurement in the same experiment[17], assuming the CCQE interaction model. Then, this tuned flux was used to measure the CCQE cross section..., of course you measure the cross section you assumed before! The danger of such procedure is, this obviously biases the measurement. The assumed of cross section model modifies the measured result. This is something we must avoid. For the data to be trusted for theorists to study their models, experimental data must be model independent as much as possible. As we will see in Sec. 4.1, MiniBooNE CCQE data suggests no discrepancy is due to the originated from the flux model, and so we do not apply any data driven correction on the neutrino flux prediction (with the exception of forward going pions, as discussed in Sec. 5.2). In a similar story, the roles of flux and cross section are swapped for the MINOS experiment. For MINOS, the majority of interactions are well-understood deep inelastic scattering (DIS). MINOS found the origin of data-simulation disagreement is from flux modeling, and meson productions are subsequently tuned in $P_T - P_z$ space by simultaneously fitting four

different beam configurations[18]. The crucial issue is how reliable are the theoretical and experimental bases of the flux and cross section models.

3. Neutrino cross section measurement

As the community moves into an era of precision measurements through detector technology advancements and the plentiful statistics afforded by high-intensity beams, an emphasis has been placed on pushing the data collected into cross sections differential in as many distributions as possible. This allows for the most stringent test of the various predictions for processes possible for a given physics sample. For MiniBooNE, the main result of the CCQE analyses is the double-differential cross section in muon kinematics. In this section, we describe the cross section measurement method step-by-step. Eq. 3 shows an example of the differential cross section of muon kinetic energy from CCQE interaction.

$$\frac{d\sigma}{dT_{\mu\,i}} = \frac{\sum_j U_{ij}\,(d_j - b_j)}{\Delta T_\mu\ \epsilon_i\,\Phi\,T}, \tag{3}$$

Here, d_j (b_j) is the data (background) reconstructed in the jth kinematic region of muon energy T_μ, U_{ij} is the probability for an event of true quantity within bin i to be reconstructed in bin j, ϵ is the detection efficiency, Φ is the integrated neutrino flux and T is the number of nuclear targets in the volume studied. We discuss each in turn.

3.1. *Signal definition*

It is very important to define what is the "signal" of the measurement precisely. It is critical especially when we want to compare the results from other experiments or thoeries. So far, we call our signal to be"CCQE" interaction, as Fig. 2 right shows. Since MiniBooNE does not have a magnetic field, there is no charge separations and the signature from muons and anti-muons are degenerate on an event-by-event basis. We can discriminate charged pions by utilising decay products, and also neutral pions by detecting electromagnetic showers. However most protons are below Cherenkov threshold and we do not discriminate. Therefore, signal topology is defined to be "1 muon + 0 pions and any number of protons".

However, there it is possible for non-CCQE channels to make this topology. Especially, when pions are absorbed in the target nuclei, CC pion production channels have intrisically same topology with CCQE. Therefore, pion production channels with nuclear pion absorption is referred "irreducible background", and the topology presented above can be called "CCQE-like" sample. After subtracting the irreducible background, data is called "CCQE" sample.

These terminologies are MiniBooNE-specific and readers should pay attention to how CCQE is defined in other experiments. In fact, it was later mentioned two-body current interaction also contributes an irreducible background. However, we

Table 1. Selection efficiency (ϵ) and purity (pur.) for the ν_μ and $\bar{\nu}_\mu$ CCQE samples. Requirements are based on well-understood lepton kinematics, and so sample selection does not suffer from the interaction model dependence.

cut #	description	ν_μ CCQE		$\bar{\nu}_\mu$ CCQE	
		ϵ	pur.	ϵ	pur.
0	no cuts	100	39.0	100	34.4
1	all subevents, # of veto hits < 6	54.8	36.8	50.8	28.5
2	1st subevent, event time window, $4400 < T(\text{ns}) < 6400$	54.3	36.8	50.4	28.6
3	1st subevent, reconstructed vertex radius < 500 cm	45.0	37.4	42.2	28.9
4	1st subevent, kinetic energy > 200 MeV	39.7	46.3	37.0	39.0
5	1st subevent, μ/e log-likelihood ratio > 0.0	36.0	62.3	35.1	52.2
6	2 subevents	29.1	71.0	31.3	59.3
7	1st subevent, $\mu - e$ vertex distance > 100 cm and $\mu - e$ vertex distance $> (500 \times T_\mu(\text{GeV}) - 100)$ cm	26.6	77.0	29.6	61.8

did not subtract them from the CCQE-like sample because we such prediction was not available at the time the analyses were performed.

3.2. *Physics sample selection, d_j*

The aim for the selection of any physics sample is to retain as many high-quality signal events while rejecting as much background as possible. Table 1 lists the requirements of the physics sample along with purity and detection efficiency figures for both ν_μ and $\bar{\nu}_\mu$ CCQE-like data sample. An important difference between the two lies in the purity, where ν_μ interactions contribute significantly to the $\bar{\nu}_\mu$ sample but not *vice versa*. It can also be seen that the $\bar{\nu}_\mu$ efficiency is around 10% higher relative to the ν_μ case subsequent to the requirement of two and only two observed subevents. The μ^- from ν_μ events not accepted by this cut have undergone nuclear capture, which is an unavoidable loss of ν_μ CCQE signal events on nuclear material when requiring the presence of the electron from μ^- decay.

While all CC ν_μ detection efficiency suffers from this nuclear capture, the lack of such interactions between μ^+ and nuclear material can be exploited as a tool to provide discrimination between ν_μ and $\bar{\nu}_\mu$ CC interactions in the absence of a magnetic field. This novel technique was first demonstrated by MiniBooNE, and is described along with other such analyses in Sec. 5.2. Detailed understanding and exploitation of μ^- nuclear capture is also important for the future of precision neutrino oscillation experiments, where the prevalent use of liquid argon detectors expose μ^-'s to a probability for nuclear capture[43] of $\sim$70%.

Broadly, this selection is entirely based on simple kinematic observations of the Cherenkov light from prompt muon and it's decay electron to ensure the CCQE events. An immediate benefit to this rather simple selection is the absence of requirements on hadronic activity. While the physics produced from studies of this sample cannot test the kinematics of hadronic behavior in CCQE interactions, the

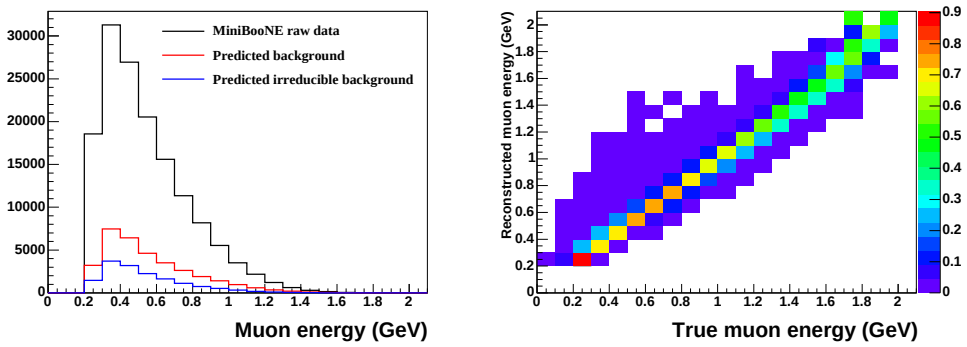

Fig. 5. The left plot shows the measured muon energy spectrum along with the total predicted background including the subset of irreducible events. The right plot shows the unsmearing matrix for muon kinetic energy. Note this matrix depends on the detector model; however in this case the dependency is weak and the resulting uncertainty is negligible compared to other errors.

selection avoids any model-dependence through assumptions of proton and neutron production and their coupling to instrumental thresholds. This is a complication common to all tracking detectors. Even with a perfect tracking detector, final-state interactions severely complicate the interpretation of such hadronic observations.

3.3. *Background subtraction, $d_j - b_j$*

The predicted background is removed from the data (Fig. 5, left). Since the process does not depend on the prediction of the signal channel, the background subtraction method, $d_j - b_j$, is recommended because it is less model dependent than purity correction method, $d_j \times \frac{s_j}{s_j+b_j}$, where predicted signal and the background in the jth bin are used to calculate the purity of the signal. Since we are measuring the CCQE cross section to allow to study theoretical CCQE models, the cross section model for the same process should not enter the formation of the physics sample.

There is one caveat of background subtraction method. In many cases the background prediction is given as a fraction of events. To reliably subtract the background, it is important to know the absolute scale of the backgrounds. This is typically obtained from side band studies and this is also the case for MiniBooNE. For MiniBooNE cross section analyses, as many irreducible backgrounds as possible are directly measured in side band samples prior to subtraction[20].

An alternative cross-section configuration involves to background subtraction at all. This can be used to obtain differential CCQE-like cross sections. Such CCQE-like data can allow studies of pion absorption channels that are important in the irreducible prediction[19].

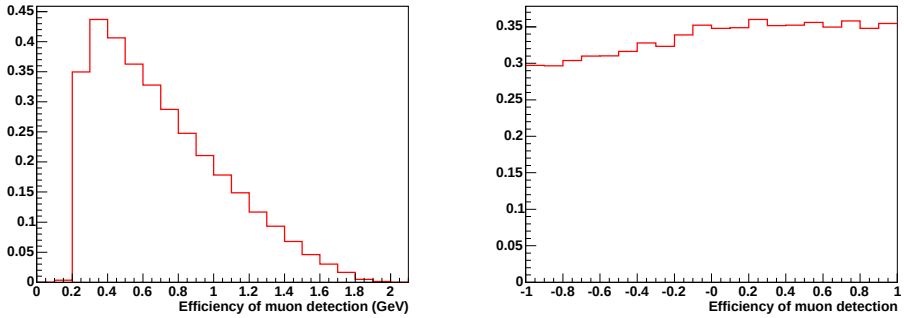

Fig. 6. These plots show the detection efficiency of muons from CCQE events in the MiniBooNE detector. In the left plot, the efficiency of forward going muons ($0.9 < cos\theta_\mu < 1.0$) is shown with function of muon kinetic energy. In the right plot, the efficiency of low energy muons ($200 < T_\mu$ (MeV) < 300) is shown with function of muon scattering angle.

3.4. *Unsmearing, U_{ij}*

The measurement is smeared due to various detector-related effects, and event selection unavoidably biases the data sample. Unfolding is the process to remove these biases. Correcting the data for these processes can be separated through the use of the unsmearing matrix U_{ij}, and accounting for the detection efficiency $\frac{1}{\epsilon_i}$. For unsmearing, the iterative Bayesian method[21] is popular for all MiniBooNE analyses [20], including $\nu_\mu(\bar{\nu}_\mu)$ CCQE analyses. This is primarily because the performance is guaranteed for any shapes and any number of bins in the distributions. This method is a Bayesian approach, which means measured data distribution is transformed to the unsmeared true distribution given by the simulation (Fig. 5, right). Therefore, the process depends on the model used to produce this unsmearing matrix. This introduces strong model dependencies for inferred variables, such as neutrino energy or 4-momentum transfer, however, biases to measured variables, such as muon energy and angle, are small. The unsmearing process is repeated with different unsmearing matrices based on different prior distributions (different CCQE models), to estimate the systematic error. In this sense, measurements using this technique can never be completely free from CCQE model dependency. Fortunately in this case the systematic error from a conservatively large range of prior distributions results in an uncertainty negligible compared to other, better understood errors. Different unsmearing techniques are studied in other analyses[22]. Unsmearing is a deep subject and future experiments are encouraged to explore further.

3.5. *Efficiency correction, ϵ_i*

The efficiency correction is applied to recovered the distribution "what if there are no cuts?" utilising efficiency, $\epsilon_i = \frac{N_i^{after\ cut}}{N_i^{before\ cut}}$, which is the ratio of signal events in

the simulation after all cuts ($N_i^{after\ cut}$) to before cuts ($N_i^{before\ cut}$). Fig. 6 show the efficiency of muons from CCQE interactions. From the left plot, one can see the efficiency drops monotonically with increasing the muon energy, simply because the detector cannot contain higher energy particles. On the other hand, right plot shows the efficiency is rather constant with muon scattering angle, because the rotationally symmetric MiniBooNE detector has uniform efficiency over scattering angles. Note there is some loss of efficiency at backward going muons due to the presence of high energy protons.

One must exercise caution with the efficiency correction. Data are often used only in limited phase space, such as in a small fiducial volume, narrow kinematic space etc. Since efficiency correction may recover events outside of that, simulation needs to be understood in the phase space in which we do not perform any measurements. For MiniBooNE CCQE analyses, we do not measure muons if kinetic energy is below 200 MeV. However, muons with energy lower than 200 MeV also contribute to the final sample due to smearing effect (the opposite is also true). Therefore it is possible to recover events in the kinematic space we do not perform measurements. Since such restoration of data heavily rely on the detector simulation, we choose not to report measurements with muon energy lower than 200 MeV. Similarly, the signal region is defined as a 550 cm radius sphere, which is smaller than the inner target volume (575 cm sphere) to avoid effects not simulated well.

3.6. *Target number and flux correction, T, Φ*

Finally, important normalization factors needed to obtain the differential cross section are the target number (T) and total flux of interaction (Φ). The total flux is the number of neutrino involved in the measurement of interest. Therefore, each measurement has a different number of total flux due to the presence of interaction thresholds. This concept is important especially to estimate the error. In general, modern wideband beam has a large error at the lowest neutrino flux distribution. However, such low energy neutrinos will not contribute to certain type of interactions such pion production channels. Therefore, taking account of threshold effects of the interaction in general give smaller flux uncertainties.

3.7. *Systematic error*

The details of systematic errors can be found elsewhere[1,2], but flux uncertainties dominate the normalization error ($\sim$9% in ν_μCCQE, $\sim$10% in $\bar{\nu}_\mu$CCQE cross section) for CCQE interactions in MiniBooNE.

Here we briefly discuss the propagation of errors. With the background subtraction method and iterative Bayesian unfolding method, the systematic error of the signal channel contributes mainly through the unsmearing matrix. In fact, signal channel MC is used to calculate efficiency, so there is some contributions on efficiency, too. However, the efficiency is defined by the ratio of signal MC after cuts to

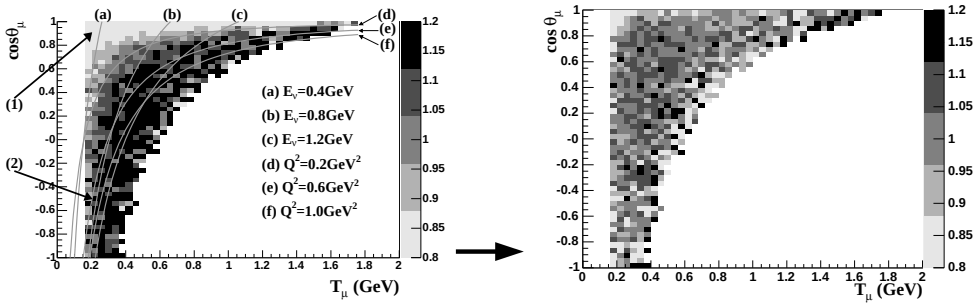

Fig. 7. Data-simulation ratio of measured CCQE events. Note simulation is normalized to data statistics.

before cuts, and many systematics cancel in this ratio. The background model affects any background removing process, and it is crucial to constrain this prediction with external data or side band measurements as much as possible. The neutrino flux error is the biggest normalization error, and mainly comes from the flux factor Φ, but also can modify the scale of the background prediction. This provides another motivation for *in situ* background measurements.

4. CCQE in ν-mode

4.1. *CCQE interaction model data driven correction*

MiniBooNE was the first experiment to collect statistics sufficient to make a detailed comparison between the observed and predicted muon kinematics for all possible production angles [23]. Presented as their ratio, the measured distribution is compared with MC simulation in Figure 7 (left). There are clear discrepancies at two regions indicated by arrows. Top left corner (region 1) shows overestimation of the simulation, and middle black band (region 2) indicate simulation underestimates the data. The questions is, what is wrong in the simulation? Since data is a convolution of neutrino flux, the neutrino cross section, and the detection efficiency, data-simulation discrepancy can be any of mis-modelling of them. However, this problem can be disentangled by following way.

Here, neutrino flux Φ is a function of neutrino energy, and cross section model σ is a function of Q^2, and as we see detector efficiency is function of muon energy T_μ. If we put all knowledge together,

$$rate \propto \int \Phi(E_\nu) \times \sigma(Q^2) \times \epsilon(T_\mu) \tag{4}$$

Now, the Fig. 7, left, has 6 curves, representing reconstructed neutrino energy E_ν^{QE} (a, b, and c) and 4-momentum transfer Q^2_{QE} (d, e, and f). The data-MC ratio plot clearly shows discrepancy along the reconstructed Q^2 lines, meaning simulation

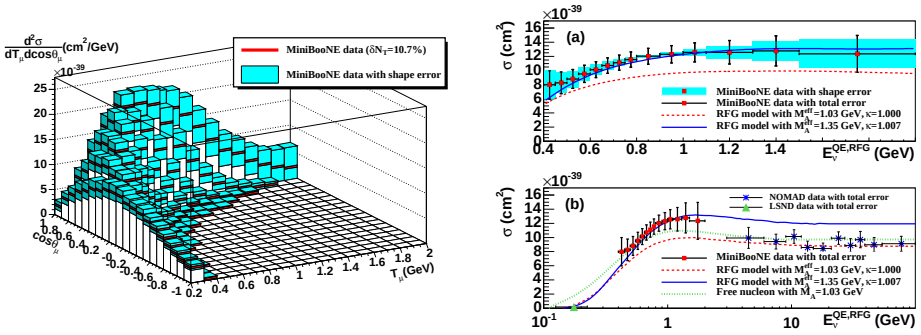
MiniBooNE data (δN_T=10.7%)
MiniBooNE data with shape error
(a)
MiniBooNE data with shape error
MiniBooNE data with total error
RFG model with M_A^eff=1.03 GeV, κ=1.000
RFG model with M_A^eff=1.35 GeV, κ=1.007
(b)
NOMAD data with total error
LSND data with total error
MiniBooNE data with total error
RFG model with M_A^eff=1.03 GeV, κ=1.000
RFG model with M_A^eff=1.35 GeV, κ=1.007
Free nucleon with M_A=1.03 GeV

Fig. 8. ν_μCCQE cross section results. Left is the flux-integrated double differential cross section, and the right is the flux-unfolded total cross section.

is wrong with function of Q^2, namely we have some problem with neutrino cross section model. This is a strong motivation to fix the CCQE cross section model. Two effective parameters are introduced in a CCQE cross section model, and as you see, simulation agree well in entire kinematic space after the correction (Figure 7, right). This parametrization was motivated purely by the practical need to have an adequate description of ν_μ CCQE events before the "box" could be opened on the ν_e CCQE candidates.

4.2. *Results*

Now, using the formula (Eq. 5), we are ready to calculate the CCQE flux-integrated double differential cross section:

$$\frac{d^2\sigma}{dT_\mu\, d\left(\cos\theta_\mu\right)_i} = \frac{\sum_j U_{ij}\left(d_j - b_j\right)}{\Delta T_\mu\, \Delta\cos\theta_\mu\, \epsilon_i\, \Phi\, T}, \tag{5}$$

This data has the highest amount of information possibly measured in this topology, with least model dependencies. Figure 8 shows the result[1]. The left plot shows the double differential cross section. An attractive feature of this result is that any theorists may simulate this by convoluting their models with given BNB flux without need of simulation software used by the experiment. The right plot shows the flux-unfolded total cross section. Although the total cross section can nicely compare the result with other experiments, reconstructing neutrino energy in MiniBooNE energy region is highly model dependent[19,24,25,26], and the comparison with theoretical models and other experiments' results need care. These plots show the clear disagreement with the relativistic Fermi gas (RFG) model. The normalization of the measured cross section is much higher than the (RFG) model with world-averaged parameters ($M_A = 1.03$ GeV).

In summary, MiniBooNE CCQE data revealed three mysteries:

- low Q^2 suppression
- high Q^2 enhancement
- large normalisation

It is still under the debate, but the community slowly understands the underlying details of these results. First, it was shown that the violation of the impulse approximation (IA) is severe at low Q^2 region[27,28]. Many interaction models are based on the IA, where a probe particle is assumed to interact with single nucleon. This approximation is broken at low momentum transfer (< 300 MeV/c), where space resolution of probe particle is larger than inter nucleon space. Some calculation, such as random phase approximation (RPA), properly takes this low energy physics into account. For the high Q^2 region, it was pointed out that interaction involved in two nucleons (two-body current), which is also neglected by IA, has an appreciable effect, and the calculation including two body currents can reproduce both high Q^2 shape and normalisation[a]. Models including RPA correction and two-body currents have been proposed[31,32], and those models show excellent agreement with the CCQE double differential data[33,34,35]. Therefore these models kill three birds with one stone!

However, this is not the end of the story. The large enhancement induced by two-body current is not always observed[36], and also models with different approaches also agree well with MiniBooNE data[37,38,39,40]. Interestingly, some models have different predictions in anti-neutrino CCQE cross sections. Therefore, now we are on the very exciting position; our task is to provide the antineutrino CCQE cross section to test these models.

5. CCQE in $\bar{\nu}$-mode

5.1. *Introduction*

Mechanically, the creation of an antineutrino beam is trivial: by reversing the polarity of the magnetic focusing horn at the proton collision station, the ν_μ parent π^+ particles are now largely deflected from the beam, and the π^- are focused toward the detector and decay to create a beam of $\bar{\nu}_\mu$. In every such antineutrino-mode setup, some important consequences arise:

- Event rates: before considering horn focusing, the leading-particle effect leads to the creation of roughly twice as many π^+ as π^-. This naturally leads to a less intense $\bar{\nu}_\mu$ beam. Moreover, $\bar{\nu}_\mu$ cross sections with matter are generally lower compared to the ν_μ case. The size of these effects are a function of energy, and at MiniBooNE the overall neutrino-mode rate

[a]The contribution of the two-body current in $\sim$1 GeV neutrino interaction is one of the most active topic in neutrino interaction physics community. We refer the reader to the growing body of literature elsewhere [29,30].

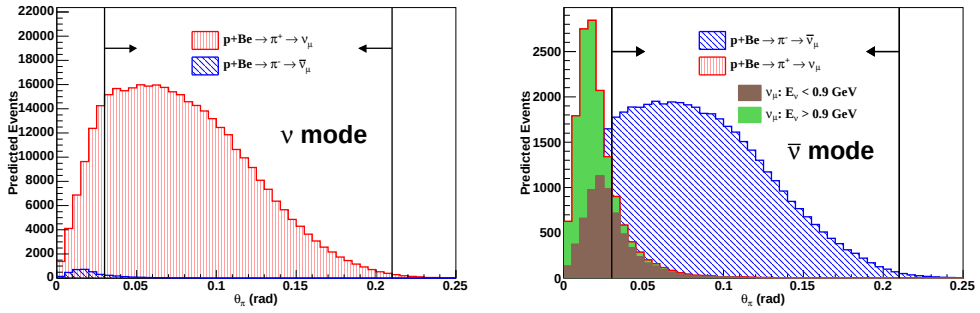

Fig. 9. Pion production angular distributions with respect to the incident proton beam (θ_π) producing ν_μ and $\bar{\nu}_\mu$ in neutrino (left) and antineutrino (right) modes. Arrows indicate the region constrained by HARP data.

difference is around five times higher compared to the antineutrino-mode rates.

- Beam energy: due also to the leading particle effect, more energy tends to be given to π^+'s compared to π^-. At MiniBooNE, the mean beam energy for neutrino (antineutrino) mode is $\sim$ 800 (650) MeV. Among other things, this has implications for neutrino oscillation measurements, where some regions of Δm^2 may be more or less challenging to measure with $\bar{\nu}$ compared to ν.
- ν_μ contamination: at least for non-magnetized detectors, by far the most experimentally-challenging feature of the antineutrino-mode beam is the natural ν_μ background. Since the event rates of ν_μ far surpass that of $\bar{\nu}_\mu$, if the horn focusing system accepts even a small amount of π^+ into the beam this may lead to large rates of ν_μ interactions in the detector.

Though the CCQE reconstruction and sample selection were well defined relatively early on in MiniBooNE's antineutrino mode data run, the final observation above had to be carefully dealt with before a $\bar{\nu}_\mu$ CCQE cross section could be extracted with any reasonable precision.

5.2. *Data driven correction on forward going pion production*

The analyses described here are available in detail elsewhere[2,42]. Here we focus on the highlights and the pieces most historically relevant, including applications to neutrino oscillation experiments looking to measure CP violation without a magnetic field.

The largest background to the $\bar{\nu}_\mu$ CCQE sample comes from ν_μ CCQE interactions. As shown by Fig. 9, these events are accepted into the antineutrino-mode beam through high-energy and forward-going π^+.

A few more remarks regarding Fig. 9:

- the antineutrino contribution to the neutrino-mode data is negligible in comparison to the converse. This is due to a convolution of flux and cross-section effects that simultaneously serve to enhance the neutrino component while the antineutrino contribution is suppressed.
- as seen in the antineutrino-mode distribution, high-energy ν_μ's are strongly correlated with the decay of π^+ created at very small opening angles. This indicates their flux is more poorly constrained by the HARP data compared to lower-energy ν_μ's. So, not only is the overall ν_μ flux in antineutrino mode highly uncertain, the accuracy of the extrapolated ν_μ flux prediction may be a function of neutrino energy.

Each of these issues will be encountered by future neutrino oscillation experiments that will observe antineutrino-mode beams though non-magnetized detectors. These complications have never before been dealt with, and so MiniBooNE's approach was an aggressive campaign to measure the ν_μ contamination with as many complementary analyses as possible. Three analyses offered comparable uncertainties and low levels of systematic correlations:

(1) **π^+ decay in ν_μCC1π^+ and π^- capture in $\bar{\nu}_\mu$CC1π^-**: The π^- produced in $\bar{\nu}_\mu$ CC1π interactions ($\bar{\nu}_\mu + N \to \mu^+ + N + \pi^-$) is captured on carbon nuclei. A key difference is the rate for stopped-π^- nuclear capture is nearly 100%, and so the simple sample selection of $1\mu + 2e$ (μ and π^+ decay chains make 2 electrons, total 3 subevents) yields a highly-pure sample of ν_μ events from which to measure their overall contribution to the antineutrino beam.
(2) **CCQE angular distribution**: In general, $\bar{\nu}_\mu$ CC interactions feature much lower momentum transfer compared to ν_μ. This leads to a kinematic restrictions for $\bar{\nu}_\mu$ compared to ν_μ, and in particular backwards-produced μ^+ are highly suppressed. Therefore, the angular distribution may be used to separate the contributions from ν_μ and $\bar{\nu}_\mu$. It should be noted that this technique depends on detailed knowledge of the $\bar{\nu}_\mu$ cross sections. Since we do not know these *a priori*, this result is not used to extract the $\bar{\nu}_\mu$ CCQE cross sections. However, as experimental and theoretical knowledge of these interactions are rapidly improving, this could be a powerful analysis in the future.
(3) **μ^- capture**: Nuclear capture of μ^- near carbon nuclei ($\sim$8%) affords a statistical asymmetry between ν_μ and $\bar{\nu}_\mu$ CCQE events. By simultaneously analyzing samples of 1μ (1 subevent) and 1μ+1e (2 subevents) sample, appreciable sensitivity is gained to the relative of μ^+ and μ^- present in each sample. Analyses of this kind could be hugely beneficial to next-generation experiments planning to use liquid argon as the detection medium [41], where the μ^- nuclear capture rate on argon is near 70%. For such a high rate and based on the presence (or lack thereof) of a decay electron, one could nearly distinguish between ν_μ and $\bar{\nu}_\mu$ interactions on an event-by-event basis without a magnetic field!

Presented as a constraint relative to the nominal prediction extrapolated from

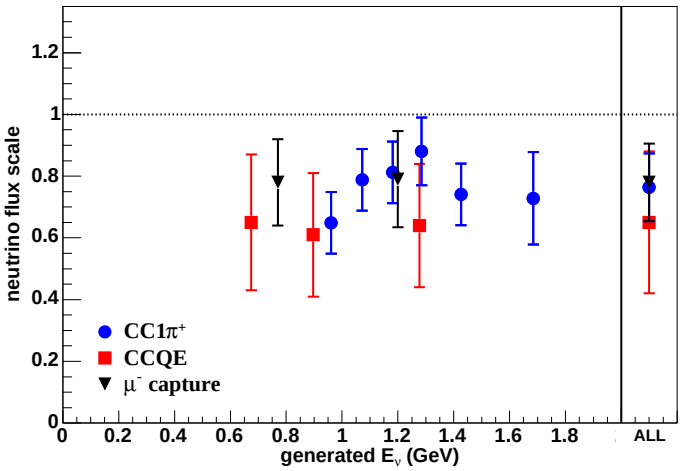

Fig. 10. Summary of the results from three techniques used to measure the ν_μ flux in the anti-neutrino mode beam.

HARP data, the final results [42] from these analyses are presented in Fig. 10.

With these constraints, the uncertainty on $\bar{\nu}_\mu$ flux from the HARP π^- production data forms the largest contribution to the overall $\bar{\nu}_\mu$ CCQE data sample. This is effectively an irreducible uncertainty to MiniBooNE, and so we turn our attention to the results.

5.3. *Results*

Fig. 11 shows a comparison of the $\bar{\nu}_\mu$ CCQE data with the various predictions from Nieves *et al.*[44], Amaro *et al.*[45], Meucci *et al.*[46], and RFG models with different parameter choices. The RFG model with world-averaged parameter ($M_A = 1.02$ GeV) reveal discrepancies found also in the behaviour of ν_μ CCQE data. Namely, a suppression of low-momentum transfer events, more cross-section strength for relatively backward-scattered muons, and a normalization excess of $\sim 20\%$.

So what does this mean? Interesting to note, the RFG parametrized with a high axial mass ($M_A = 1.35$ GeV) seems to do remarkably well describing the antineutrino data. While the nuclear model assumed in the RFG is rather naive, apparently the interplay between axial and vector pieces in this model is grossly correct. This is at least true at the energies probed by MiniBooNE ($E_\nu \sim 700$ MeV), however, recent data from MINERνA suggest that this breaks down at higher energies ($E_\nu \in 1.5 - 10$GeV) [47,48].

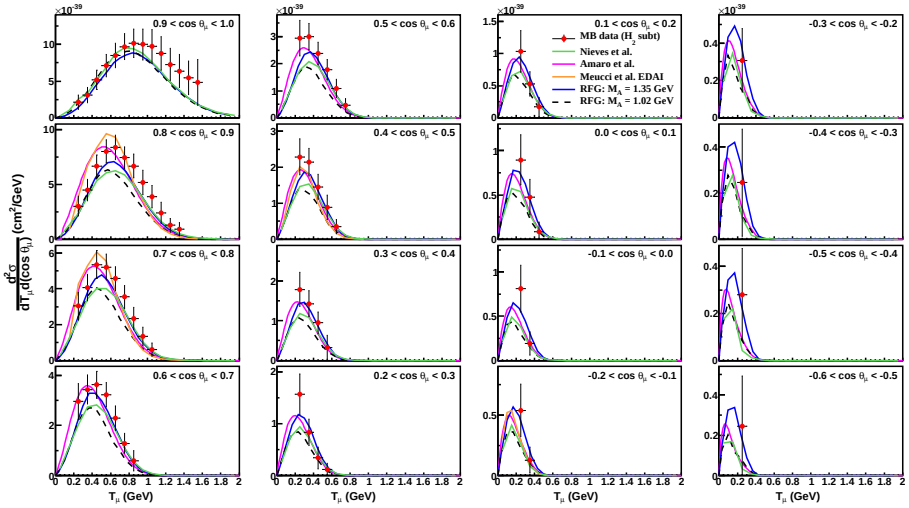
MB data (H$_2$ subt)
Nieves et al.
Amaro et al.
Meucci et al. EDAI
RFG: M$_A$ = 1.35 GeV
RFG: M$_A$ = 1.02 GeV
0.9 < cos θ$_\mu$ < 1.0
0.8 < cos θ$_\mu$ < 0.9
0.7 < cos θ$_\mu$ < 0.8
0.6 < cos θ$_\mu$ < 0.7
0.5 < cos θ$_\mu$ < 0.6
0.4 < cos θ$_\mu$ < 0.5
0.3 < cos θ$_\mu$ < 0.4
0.2 < cos θ$_\mu$ < 0.3
0.1 < cos θ$_\mu$ < 0.2
0.0 < cos θ$_\mu$ < 0.1
-0.1 < cos θ$_\mu$ < 0.0
-0.2 < cos θ$_\mu$ < -0.1
-0.3 < cos θ$_\mu$ < -0.2
-0.4 < cos θ$_\mu$ < -0.3
-0.5 < cos θ$_\mu$ < -0.4
-0.6 < cos θ$_\mu$ < -0.5
d^{2}σ / dT$_\mu$d(cos θ$_\mu$) (cm^2/GeV)
T$_\mu$ (GeV)

Fig. 11. The $\bar{\nu}_\mu$ CCQE flux-integrated double-differential cross section compared to various predictions.

6. Combined measurements of ν_μ and $\bar{\nu}_\mu$ CCQE

With the high-statistics MiniBooNE ν_μ and $\bar{\nu}_\mu$ CCQE measurements described here, an opportunity exists to extract even more information by taking the difference or the ratio of them. The cross section ratio is sensitive to the relative contribution of this term in the cross section. For the total cross section, these ratio and difference distributions are presented in Figure 12, and compared with theoretical predictions from Amaro *et al.*[45], Bodek *et al.*[37], Martini *et al.*[49,50], Nieves *et al.*[44], Meucci *et al.*[46], along with the RFG and the parameter choice $M_A = 1.35$ GeV. While it is interesting to test the overall normalization of the observed ν_μ and $\bar{\nu}_\mu$ CCQE cross sections with more modern ideas of nuclear physics, a much more rigorous test is available with comparisons of the same quantities with the double-differential cross sections. The observed combined measurements of ν_μ and $\bar{\nu}_\mu$ CCQE are shown in Figure 13. As this analysis combines information from both ν_μ and $\bar{\nu}_\mu$ CCQE processes while fully exploiting systematic uncertainties, this is the most powerful measurement of CCQE interactions possible with the MiniBooNE detector.

Note that the ratio $\frac{\sigma_{\nu_\mu}}{\sigma_{\bar{\nu}_\mu}}$ tests the relative normalization, while the difference $\sigma_{\nu_\mu} - \sigma_{\bar{\nu}_\mu}$ is sensitive to the absolute strength of the cross sections. Therefore there is some independent information between these tests, and any description must be consistent with both measurements of the combined cross sections. The difference $\nu_\mu - \bar{\nu}_\mu$ is in principle proportional to the interference term between the axial and vector pieces of the formalism for CCQE interactions. This is true even including nuclear effects. Furthermore, this term is also proportional to the transverse response, and it may

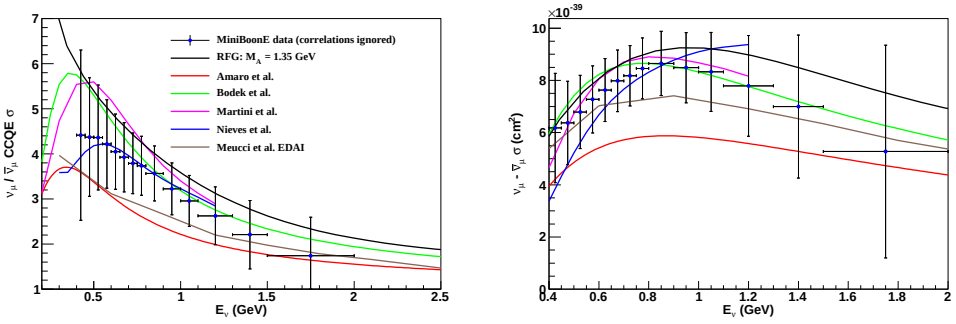

Fig. 12. Ratio (left) and difference (right) between MiniBooNE ν_μ and $\bar{\nu}_\mu$ CCQE flux-unfolded total cross section data compared to various predictions. Note errors of two data sets are added by quadrature.

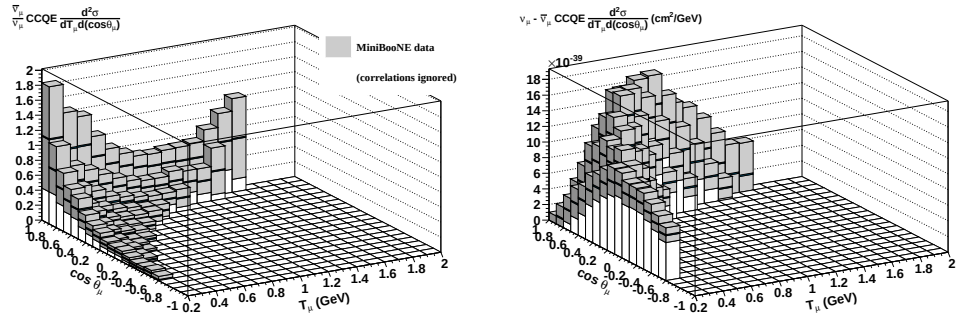

Fig. 13. Ratio (left) and difference (right) between MiniBooNE ν_μ and $\bar{\nu}_\mu$ CCQE flux integrated double differential cross section data. Note errors of two data sets are added by quadrature.

be useful to study nuclear effects sensitive to the transverse response.

7. Conclusion

The CCQE interaction is enormously important in both the history and future of neutrino physics. It is a rather simple interaction that has recently revealed a rich nature. MiniBooNE observed structures of this interaction in unprecedented detail, and we are waiting further information both from theories and experiments to further refine this story. This is of course critical to move towards a rigorous understanding of the underlying mechanisms, but their accurate description may also soon serve a practical purpose critical to next-generation neutrino oscillation experiments such as T2K [51], NOνA [52], and LBNE [53] by providing independent information for the interaction channel use most prevalently to search for oscillations.

References

1. A. A. Aguilar-Arevalo *et al.*, Phys. Rev. D **81**, 092005 (2010).
2. A. A. Aguilar-Arevalo *et al.*, Phys. Rev. D **88**, 032001 (2013).
3. C. Athanassopoulos *et al.*, Phys. Rev. Lett. **75**, 2650 (1995).
4. A. A. Aguilar-Arevalo *et al.*, Phys. Rev. D **79**, 072002 (2009).
5. A. A. Aguilar-Arevalo *et al.*, Nucl. Instrum. Meth. A **599**, 28 (2009).
6. K. Abe *et al.* [T2K Collaboration], Phys. Rev. D **87**, 092003 (2013).
7. R. B. Patterson *et al.*, Nucl. Instrum. Meth. A **608**, 206 (2009).
8. A. A. Aguilar-Arevalo *et al.*, Phys. Rev. D **81**, 013005 (2010).
9. A. A. Aguilar-Arevalo *et al.*, Phys. Rev. D **82**, 092005 (2010).
10. A. A. Aguilar-Arevalo *et al.*, arXiv:1309.7257 [hep-ex].
11. A. A. Aguilar-Arevalo *et al.*, Phys. Rev. D **83**, 052007 (2011).
12. A. A. Aguilar-Arevalo *et al.*, Phys. Rev. D **83**, 052009 (2011).
13. J. A. Formaggio and G. P. Zeller, Rev. Mod. Phys. **84**, 1307 (2012).
14. A. A. Aguilar-Arevalo *et al.*, Phys. Rev. D **79**, 072002 (2009).
15. K. Abe *et al.* [T2K Collaboration], Phys. Rev. D **87**, 012001 (2013).
16. M. G. Catanesi *et al.* [HARP Collaboration], Eur. Phys. J. C **52**, 29 (2007).
17. N. J. Baker *et al.*, Phy. Rev. D **25**, 617 (1982).
18. Z. Pavlovic, FERMILAB-THESIS-2008-59.
19. O. Lalakulich, U. Mosel and K. Gallmeister, Phys. Rev. C **86**, 054606 (2012)
20. Teppei Katori [MiniBooNE and SciBooNE Collaborations], arXiv:1304.5325 [hep-ex].
21. G. D'Agostini, Nucl. Instrum. Meth. A **362**, 487 (1995).
22. C. Anderson, FERMILAB-THESIS-2010-49.
23. A. A. Aguilar-Arevalo *et al.*, Phys. Rev. Lett. **100**, 032301 (2008).
24. M. Martini, M. Ericson and G. Chanfray, Phys. Rev. D **85**, 093012 (2012).
25. M. Martini, M. Ericson and G. Chanfray, Phys. Rev. D **87**, 013009 (2013).
26. J. Nieves *et al.*, Phys. Rev. D **85** (2012) 113008.
27. A. V. Butkevich and S. P. Mikheyev Phys. Rev. C **72**, 025501 (2005).
28. Artur M. Ankowski, Omar Benhar, and Nicola Farina, Phys. Rev. D **82**, 013002 (2010).
29. H. Gallagher, G. Garvey, and G. P. Zeller, Annu. Rev. Part. Sci. 2011.61:355 (2011)
30. J. G. Morfn, J. Nieves, and J. T. Sobczyk, AHEP, vol. 2012, ID 934597, (2012)
31. M. Martini, M. Ericson, G. Chanfray and J. Marteau, Phys. Rev. C **81**, 045502 (2010).
32. J. Nieves, I. Ruiz Simo and M. J. Vicente Vacas, Phys. Lett. B **707**, 72 (2012).
33. M. Martini, M. Ericson and G. Chanfray, Phys. Rev. C **84**, 055502 (2011).
34. J. Nieves, I. Ruiz Simo and M. J. Vicente Vacas, Phys. Lett. B **707**, 72 (2012).
35. O. Lalakulich, K. Gallmeister and U. Mosel, Phys. Rev. C **86**, 014614 (2012).
36. J. E. Amaro *et al.*, Phys. Rev. D **84**, 033004 (2011).
37. A. Bodek, H. S. Budd and M. E. Christy, Eur. Phys. J. C **71**, 1726 (2011).
38. Jan T. Sobczyk, Eur. Phys. J. C **72**, 1850 (2012).
39. A. Meucci *et al.*, Phys. Rev. Lett. **107**, 172501 (2011).
40. A. V. Butkevich, Phys. Rev. C **82**, 055501 (2010).
41. A. de Gouvea *et al.*, arXiv:1310.4340 [hep-ex].
42. A. A. Aguilar-Arevalo *et al.*, Phys. Rev. D **84**, 072005 (2011).
43. A. Klinskih *et al.*, AIP Conf. Proc. **942**, 49 (2007).
44. J. Nieves, I. Ruiz Simo and M. J. Vicente Vacas, Phys. Lett. B **721**, 90 (2013).
45. J. E. Amaro *et al.*, Phys. Rev. Lett. **108**, 152501 (2011).
46. Andrea Meucci and Carlotta Giusti, Phys. Rev. D **85**, 093002 (2012).
47. G. A. Fiorentini *et al.*, Phys. Rev. Lett. **111**, 022502 (2013).
48. L. Fields *et al.* (MINERνA Collaboration), Phys. Rev. Lett. **111**, 022501 (2013).
49. M. Martini, M. Ericson, G. Chanfray, and J. Marteau, Phys. Rev. C **81**, 045502 (2010).

50. M. Martini and M. Ericson, Phys. Rev. C **87**, 065501 (2013).
51. K. Abe *et al.* [T2K Collaboration], Phys. Rev. D **88**, 032002 (2013).
52. M. D. Messier [NOvA Collaboration], arXiv:1308.0106 [hep-ex].
53. C. Adams *et al.* [LBNE Collaboration], arXiv:1307.7335 [hep-ex].